



# EBSD-coupled indentation: nanoscale mechanics of lithium metal

Jack Aspinall<sup>a, b</sup>, David E.J. Armstrong<sup>a, b, \*\*, \*</sup>, Mauro Pasta<sup>a, b, \*</sup>

<sup>a</sup> Department of Materials, University of Oxford, Parks Road, Oxford OX1 3PH, United Kingdom

<sup>b</sup> The Faraday Institution, Quad One, Didcot, OX11 0RA, United Kingdom

## ARTICLE INFO

### Article history:

Received 4 September 2022

Received in revised form

12 October 2022

Accepted 15 October 2022

Available online 27 October 2022

### Keywords:

Mechanics

Lithium dendrite

Nanoindentation

EBSD map

Solid state

surface preparation

## ABSTRACT

The fracture of ceramic solid electrolytes, driven by the plating of lithium within cracks, has been identified as one of the fundamental issues to successfully develop solid-state batteries. Understanding the mechanics of lithium at the nanoscale is therefore essential. In this work, the elastic and plastic properties of lithium are measured by nanoindentation within an electron microscope. Lithium metal samples are characterized by electron backscattered diffraction before and after indentation to understand the dependence of the mechanical properties on crystallographic orientation and determine the stiffness tensor components, moduli, and Poisson's ratio using a method first proposed by Vlassak and Nix. The measured stiffness tensor components are  $C_{11} = 13.3$ ,  $C_{12} = 11.2$ , and  $C_{44} = 8.8$  GPa. Hardness measurements show a clear size effect with hardness in excess of 100 MPa observed for indent depths below 300 nm, which could contribute toward observed lithium filament propagation.

© 2022 The Author(s). Published by Elsevier Ltd. This is an open access article under the CC BY license (<http://creativecommons.org/licenses/by/4.0/>).

## 1. Introduction

The fracture of solid electrolytes by lithium metal filament penetration is a well-documented failure mode of lithium metal batteries [1–3]. Yet it seems counterintuitive for filaments of lithium metal, one of the softest metals [4], to be able to fracture stiff ceramics. The fracture process in lithium metal batteries is inherently a nanoscale effect. By directly probing the mechanical properties of lithium using nanoindentation, we can better understand the mechanical interaction occurring between lithium metal and the solid electrolyte.

The mechanical response of lithium consists of a recoverable/elastic component and a permanent/plastic component. Lithium's elastic response is fully described by its stiffness tensor  $C$ , which has three independent components  $C_{11}$ ,  $C_{12}$ , and  $C_{44}$ . The tensor allows the resultant elastic strain to be calculated from any given stress tensor. Elasticity is independent of length scale. Four works have measured the three independent elastic constants of lithium ( $C_{11}$ ,  $C_{12}$ , and  $C_{44}$ ), which together fully describe the material's anisotropic elastic response [5–8]. Overall, these works suggest tensor components in the range

$C_{11} = 12.3$ – $14.5$  GPa,  $C_{12} = 10.2$ – $11.3$ , and  $C_{44} = 8.5$ – $8.9$  GPa. This suggests lithium is a highly elastically anisotropic material ( $A \approx 8$ ). Most mechanical works on lithium metal have studied polycrystals, with Young's modulus values ranging from 4.97 GPa [9] to 9.8 GPa [10]. Notably several studies have measured values close to 7.8 GPa [11–13]. Given lithium's high elastic anisotropy, it is surprising that there is such strong agreement between measurements of polycrystalline Young's modulus in studies with different sample preparation and testing methodologies. Taking the average of prior single crystal studies ( $C_{11} = 13.4$ ,  $C_{12} = 11.0$ ,  $C_{44} = 8.7$  GPa) gives a Hill estimate of 10.8 GPa, which is typically a good estimate for untextured polycrystalline moduli [14]; 7.8 GPa lies 28% below this expected value. The disparity between single crystal and polycrystal elastic properties as well as the range of single-crystal values reported in the literature justifies new work quantifying the stiffness tensor.

Lithium's plastic response is complex, depending on the mobility of micron-scale dislocations. At small length scales relevant for lithium filaments, the number of dislocations within the stressed volume is limited, and therefore, size-dependent hardness is expected. Several works have studied plasticity in lithium in micron-scale to bulk samples and at a range of strain rates. This is summarized well in the recent paper by Fincher et al. [15]. Collectively, studies find bulk lithium has a yield stress of 0.6 MPa, increasing by around a factor of two with high strain rate [12,13,15–17].

\* Corresponding author.

\*\* Corresponding author.

E-mail addresses: [david.armstrong@materials.ox.ac.uk](mailto:david.armstrong@materials.ox.ac.uk) (D.E.J. Armstrong), [mauro.pasta@materials.ox.ac.uk](mailto:mauro.pasta@materials.ox.ac.uk) (M. Pasta).

With decreasing plastic zone size, the hardness of lithium increases by over an order of magnitude. Xu et al. performed nano-pillar compression to investigate size-dependent hardness, measuring an increase in yield stress from 15 to 105 MPa [8] as pillar size decreases from 9.45  $\mu\text{m}$  to 1.39  $\mu\text{m}$ . The pillars were prepared by focused ion beam milling which raises concerns that ion-implantation from pillar machining [18] is contributing to an increase in hardness, especially for the small pillars. In typical materials such as molybdenum, the effect of ion-beam damage on measured mechanical properties is negligible [19], but due to lithium's low atomic mass, the penetration depth of focused ion beam milling ions is significantly higher. Our stopping range of ions in matter (SRIM [20]) calculations suggest a mean ion implantation depth of  $102 \pm 20$  nm in Li compared to  $11 \pm 6$  nm in Mo with a 30 kV  $\text{Ga}^+$  beam. The phase diagram of lithium and gallium is complex with many intermetallics that may form [21]. The contribution of this focused ion beam milling-damaged shell to the observed hardness is unclear. Nevertheless, the trend agrees with microindentation work [10,15] and similar experiments on other metals [22]. In the submicron region relevant for lithium filament initiation, there is a broad spread of results, with yield stress varying from 8 MPa [10] to over 100 MPa [8] between different studies. More work is needed at this length scale to quantify size-dependent plasticity in lithium metal.

A summary table of room temperature lithium metal mechanical properties studies is available in the appendix (Table S1).

In this work, using a nanoindenter within a scanning electron microscope (SEM), we have correlated nanoindentation with electron backscattered diffraction (EBSD) mapping of lithium metal to allow the orientation dependence of the mechanical response to be measured at the nanoscale. Using well established mathematics [23], these measurements have allowed us to calculate the elastic stiffness tensor of lithium, getting values of  $C_{11} = 13.3$ ,  $C_{12} = 11.2$ , and  $C_{44} = 8.8$  GPa. We simultaneously measure hardness and observe strong size dependence, with hardness in excess of 100 MPa observed for indent depths below 300 nm. We discuss the impact of these results on lithium filament propagation into stiff ceramic electrolytes.

## 2. Materials and methods

### 2.1. Electron microscopy

SEM characterization and nanoindentation were performed within a single contained system consisting of a Bruker Hysitron PI88 in-situ nanoindenter, with a five-axis sample stage mounted to the five-axis stage of a Tescan Mira-3 FEG-SEM with Oxford Instruments EBSD and energy dispersive x-ray spectroscopy (EDX) detectors. The SEM chamber opens into a dedicated MBraun argon glove box, enabling sample change without air exposure. EBSD was performed at a beam voltage of 20 kV, current of 500 nA, tilt of 70°, and a working distance of 15 mm. The two five-axis stages of the indentation setup allow the sample to be rotated between EBSD and indentation positions. The system allows indents to be performed at distinct sites. Only large grains with good EBSD band contrast were tested, and any indents accidentally placed on or near grain boundaries were excluded from analysis.

### 2.2. Lithium sample preparation

All work was performed within MBraun glove boxes ( $<0.1$  ppm  $\text{O}_2$  and  $\text{H}_2\text{O}$ ). To prepare the lithium samples, 0.5 g of lithium metal foil (Alfa Aesar, 99.9% foil) was melted at 250° C within a custom-made stainless steel crucible, lined with stainless steel foil and with a stainless steel lid, in a furnace (MTI OTF-1200X-S-II) within a glove box, before removing from the furnace to air cool. The stainless steel liner was peeled away to extract the solidified ingot. Test samples of approximate size 5 mm  $\times$  5 mm  $\times$  2 mm were cut from the center of the ingots using a scalpel and mounted to 5 mm aluminum SEM stubs using a small amount of two-part epoxy (Araldite). Surfaces were prepared using fresh polytetrafluoroethylene-coated microtome blades (EpreDia™ Shandon™) with a table-top vice as a guide. The cut sample surface was aligned perpendicular to the indentation axis using the SEM optics to within 0.5° in both tilt axes. Atomic force microscopy (AFM) measurements gave a surface roughness of  $38 \pm 2$  nm for a 25- $\mu\text{m}$  square scan size.

### 2.3. Indentation

Indentation was performed using a Bruker PI88 in-situ nanoindenter, with a diamond Berkovich indentation tip (Hysitron), which was scanned with the AFM to extract a cross-sectional area function used in the calculation of reduced modulus and hardness from the measured stiffness, displacement, and load. The tip was cleaned before each test under an optical microscope. The nanoindenter was carefully calibrated to ensure quantitatively accurate results. Machine compliance was measured to be 8.02 nm/mN. Prior to each test, thermal drift rate was measured in contact, with preload of 10  $\mu\text{N}$ , over 40 s. The first 20 s was given as time for the system to stabilize after initial contact, and the last 20 s sampled to calculate mean drift rate, assumed constant throughout the test. Both modulus and hardness values were obtained using the continuous stiffness measurement technique. A continuous modulus stiffness measurement frequency of 70 Hz was used, as it gave the lowest spread in phase shift and displacement amplitude, of frequencies from 30 to 300 Hz. A large dynamic load amplitude of 50  $\mu\text{N}$  at a target quasistatic load of 1000  $\mu\text{N}$  was used scaling with the square root of quasistatic load to minimize viscoplasticity error while retaining indenter contact [24,25]). Because the continual stiffness measurement method captures both the load and unload segment of the oscillation, the effect of creep on measured stiffness is small. Indentation modulus values were obtained by averaging the stiffness measured between 1000 nm and 1500 nm of depth – with the indentation modulus ( $M$ ) calculated using an adapted version of the equation presented by Oliver and Pharr [26] for anisotropic materials (Equation (1)). Due to lithium's  $M/H$  value being so large, the choice of epsilon used to calculate the contact area ( $A_c$ ) makes negligible difference to the values of indentation modulus, so the standard 0.75 is used. We observed no pile up either by in-situ SEM or by AFM; therefore, no pile-up correction was applied. The measured moduli of each of the indents within a grain were averaged to give a mean value of indentation modulus for each grain.

**Table 1**

Elastic properties results for pure lithium metal tested by nanoindentation.  $\nu$ , B, E, and G are values for untextured lithium polycrystalline sample properties, with the two values being the Reuss and Voigt estimates, respectively. All values are given in GPa, except A and  $\nu$  that are dimensionless.

Property	C11	C12	C44	E[100]	E[111]	A	$\nu$	B	E	G
Value	13.34	11.19	8.83	3.1	21.2	8.21	0.28/0.41	11.9	6.41/14.81	2.27/5.73

$$M = \frac{\sqrt{\pi}}{2} \frac{S}{\sqrt{A_c}} \quad (1)$$

## 2.4. Data processing

EBSD data were processed using Oxford Instruments Aztec software, and the MTEX Matlab package, giving orientation data as a set of 3 Euler angles following the anticlockwise rotation ZX'Z" convention. Nanoindentation data were processed with Bruker's Triboscan software and Matlab, and inverse pole figure graphs plotted with the MTEX Matlab package. Reuss and Voigt estimates were also calculated with MTEX. The elastic stiffness tensor was calculated using the mathematics described by Vlassak and Nix [23] implemented in a Nelder–Mead minimization algorithm, details are available in the appendix.

## 3. Results and discussion

Using very sharp microtome blades, we were able to prepare fresh lithium surfaces, with a surface roughness of  $38 \pm 2$  nm (Table S2), which we were able to successfully EBSD (Fig. 1A). The coloring of each pixel denotes the crystal lattice orientation relative to the sample normal at that point, calculated from the Kikuchi diffraction pattern (Fig. 1B). The orientation is shown in the inverse pole figure (Fig. 1C). This preparation method may be useful for other studies on lithium, such as in the preparation of samples for AFM [27] or ex-situ solid electrolyte interphase (SEI) formation and characterization. In the map shown in Fig. 1A, 78% of the 29400 points indexed successfully. It can be observed from the map that points near lateral grain boundaries are rarely resolved. Electron cross section scales strongly with atomic number [28], so lithium having the lowest electron cross section of all metals represents a limit case for EBSD, with large electron interaction volumes and low-contrast diffraction patterns. A detailed discussion of the implications for this on EBSD mapping, including modeling of the electron interaction volume, is provided in the appendix.

Having successfully EBSD mapped lithium metal samples, arrays of indents were performed within large grains. Fig. 2A and B shows an example indent array's continuous stiffness measure of modulus and the array's corresponding EBSD map. A schematic of the experiment is shown in Fig. 2C. By averaging the modulus data for

each set, we can obtain a point in surface orientation – modulus space, as shown on the inverse pole figure in Fig. 2D. The averages of measured indentation modulus for multiple indentations within grains of differing orientation, plotted in Fig. 2D, show the expected trend of mechanical indentation anisotropy for cubic crystals, with indents along vectors near the  $\langle 100 \rangle$  axis of the crystal having lower moduli (11 GPa) than those near the  $\langle 111 \rangle$  direction (14 GPa). A Nelder–Mead minimization algorithm was used to obtain a least squares fit, giving fitted values of the stiffness tensor of  $C_{11} = 13.3$ ,  $C_{12} = 11.2$ , and  $C_{44} = 8.8$  GPa (see appendix for details).

To visualize the resultant fit, the indentation modulus curve for grains with surface normals lying in the (110) plane has been calculated, with its maximum along the  $\langle 111 \rangle$  vector at  $54^\circ$  as shown in Fig. 2E. The eight experimental grain orientations with surface normal lying near the {110} planes (top and right edges of D) have also been plotted. The error bars represent the standard deviation of the indentation modulus values for the indents within each grain's indent set. The three stiffness matrix components fully describe the elastic response of the material, and other values such as polycrystalline Young's, shear, and bulk moduli can be calculated from them (see Table 1). In the table, the two extreme single crystal uniaxial Young's moduli values in the [100] and [111] directions have been calculated with approximately a factor of seven difference.

Our elastic stiffness tensor results sit in the middle of the range of measured/calculated indentation results [6–8] and are in very good agreement with the work by the group of Slotwinski and Felice [6,7]. The work shows lithium is highly elastically anisotropic. Implementing the full stiffness tensor (measured in this work) allows the elastic response of the material to be precisely determined across length scales for any general stress state, with numerical tools such as Abaqus. The knowledge of lithium's elastic anisotropy also allows worst-case mechanical scenarios to be modeled, e.g., single-crystal lithium filaments compressed in the [111] direction will act differently to those compressed in the [100] direction.

Practically, lithium's high elastic anisotropy and large grain size means that the stiffness of the material is strongly dependent on the texture. The Reuss and Voigt estimates for polycrystalline Young's moduli of lithium using our measured values are 6.41 GPa and 14.81 GPa. We would therefore reasonably expect a true polycrystal to have a Young's modulus of 10.6 GPa (arithmetic mean). The significant difference between the two estimates shows

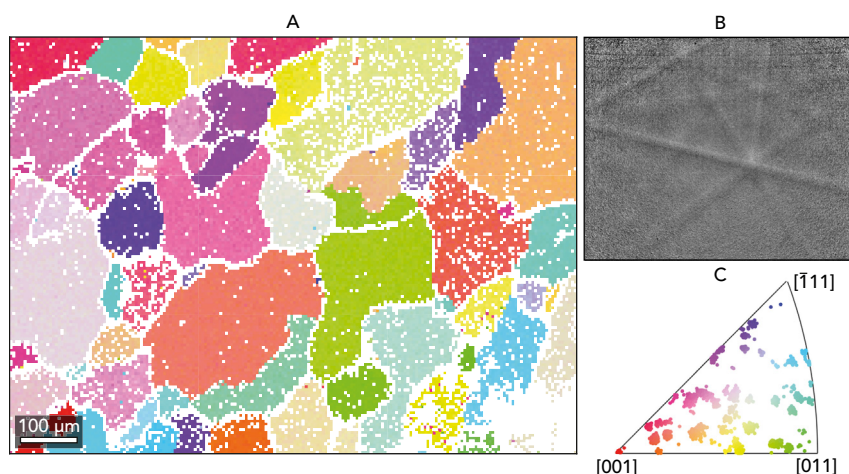


**Fig. 1.** Electron backscattered diffraction (EBSD) of lithium metal. A - EBSD map showing large, equiaxed grains of lithium metal. B - Example Kikuchi pattern imaged by EBSD detector. C - Inverse pole figure for shown map showing orientation of crystal lattice for points in the map.

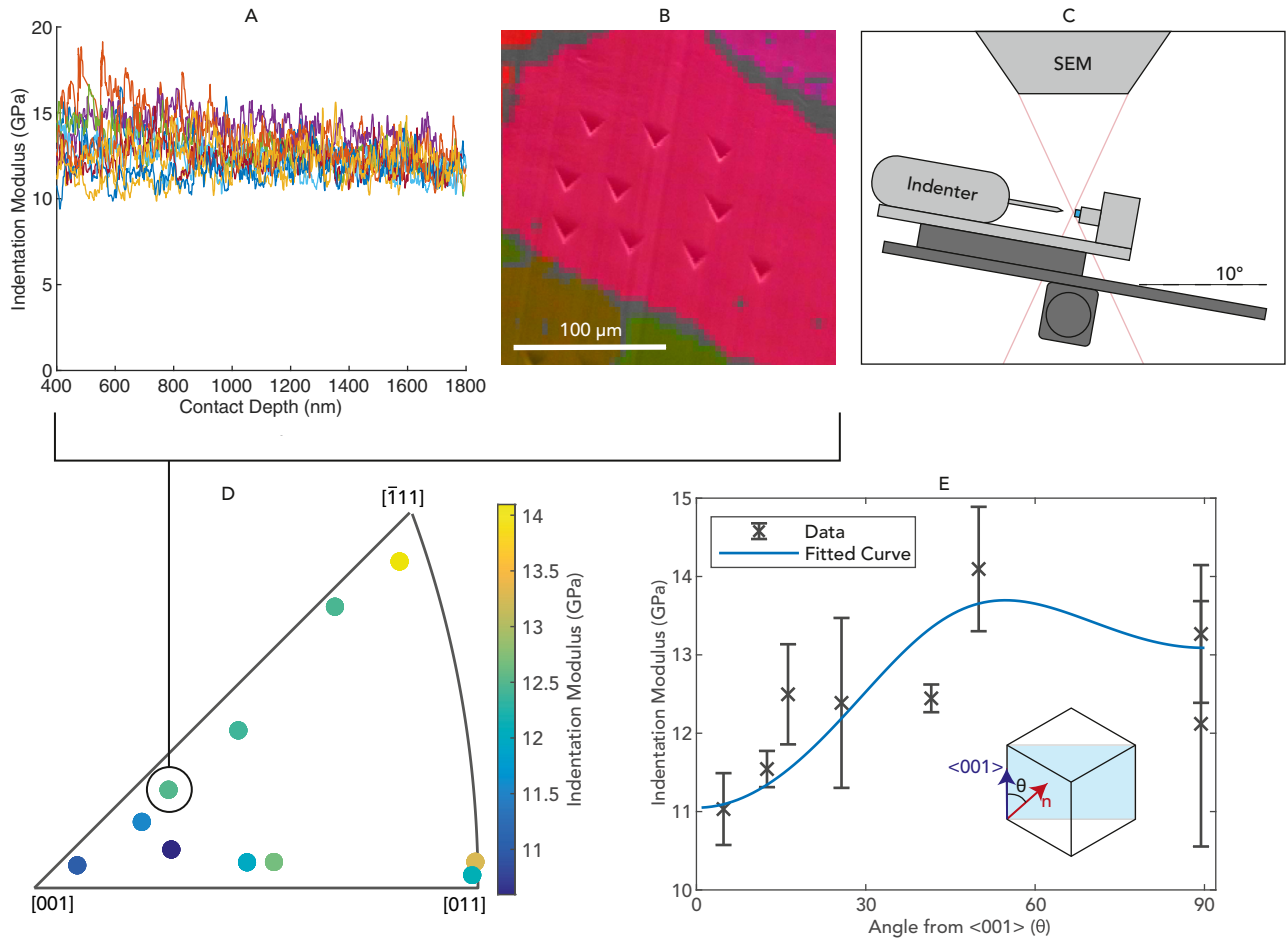


**Fig. 2.** Orientation-dependent elastic moduli of lithium metal. A – Measured indentation modulus vs. depth for one grain. B – Corresponding electron backscattered diffraction map superimposed on scanning electron microscope image of indented grains. C – Schematic showing experimental setup during indentation. D – Indentation modulus inverse pole figure showing orientation dependence of measured indentation modulus. E – Measured moduli for the eight indented grains with surface normal near {110} planes plotted against angle from <001> vectors, predicted trendlines from previous stiffness data and this works best-fit result plotted. Schematic inset in E to shows theta definition.

that the arrangement of grains of different orientations can have a substantial effect on the sample's modulus – this is confirmed by the wide range of literature values for stiffness of polycrystalline lithium summarized in the appendix table (Table S1). Due to its softness, lithium is typically prepared by rolling which induces strong [100] out-of-plane texture into the material [29], a direction in which its stiffness is much lower. The different polycrystalline moduli values obtained in the literature can be explained by the expected texture in the samples based on the processing method such as wire drawing or foil rolling [17], the large grain size of lithium ( $\approx 100 \mu\text{m}$  [30]), and the error in the measurements.

The continuous measurement technique gives hardness (load/contact area) with depth, throughout the indentation. This provides a good approximation for the stresses evolved during rapid lithium plating within a crack. As can be seen in Fig. 3A, there is a strong depth dependence on the measured hardness due to the size of indentation being of the same magnitude as a dislocation. Such depth dependence is well described by the equation first put forward by Nix and Gao in 1998 (Equation (2) [31]), tending to a hardness of  $H_0$  at high depth, with a characteristic decay length  $h^*$ . When fitting the data beyond 500 nm, where the indentation error is small, the hardness curves for all indents follow this expression. At low depths (<500 nm), where deviation from this trend is often

observed [32], measured hardness values slightly exceed the curve. The average values for all indents, and the standard deviations are  $H_0 = 2.01 \pm 0.16 \text{ MPa}$  and  $h^* = 97.8 \pm 42.1 \mu\text{m}$ .

$$H = H_0 \sqrt{1 + \frac{h^*}{h}} \quad (2)$$

As can be seen in Fig. 3A, hardness curves from different grain orientations are very similar, but a slight hardness anisotropy between lattice orientations is observed, with the average hardness between 1.2 and 1.5  $\mu\text{m}$  for each indentation direction varying from 22.3 MPa in the <111> indentation axis to 17.2 MPa near <100>, as plotted in Fig. 3A, with the corresponding points on the inverse pole figure circled (Fig. 3B). The measured anisotropy of hardness corresponds well with the calculated Schmid factor of the axis of indentation, for the {110} <111>, {112} <111>, and {123} <111> slip systems of the body-centered cubic crystal structure – as shown in Fig. 3C. Where the Schmid factor is low, the hardness is high. This is intuitive, given the critically resolved shear stress on the slip plane is proportional to the Schmid factor and the applied stress; therefore, for a lower Schmid factor, a larger normal force is needed to drive slip [33].



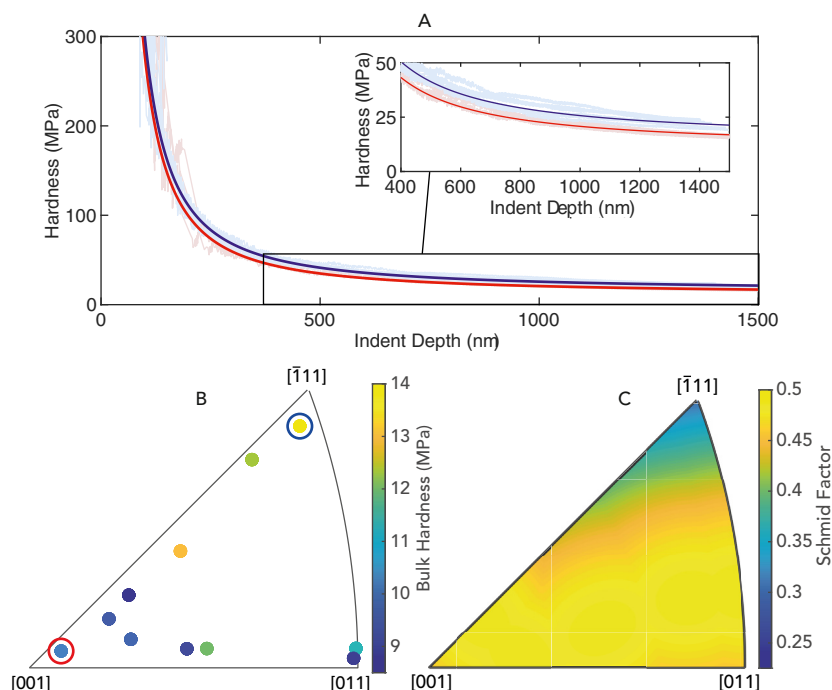


**Fig. 3.** Size and orientation dependent hardness of lithium metal measured by nanoindentation. A – Measured hardness vs. indentation depth for indents in grains near [100] and [111] as highlighted in B. B – Inverse pole figure showing orientation dependence of measured hardness averaged between 1.2 and 1.5  $\mu\text{m}$ . C – Inverse pole figure showing Schmid factor of lithium metal assuming equal activation energy on {110}, {123} and {112} slip planes.

We observed adhesion between the indentation tip and the sample, such that a negative load was needed to detach the tip from the sample. The mean value of this pull-off force was  $-532.6 \pm 0.8 \mu\text{N}$  and mean pull-off stress was  $7.95 \pm 0.02 \text{ MPa}$ . No clear trend with orientation was observed. Published work on Berkovich indentation adhesion is limited to ideal elastic systems such as polydimethylsiloxane [34], so the mathematics is not applicable for plastic materials such as lithium. Approximating the indenter as a rigid flat punch ( $r = \sqrt{A_c/\pi}$ ), and using the Kendall model ( $P_{\text{off}} = 8A_c M W_{\text{ad}} R$ ) [35], the work of adhesion is  $9.61 \pm 0.03 \text{ mJ/m}^2$ . This should only be taken as an estimate. We are not aware of any other quantitative reports of adhesion with lithium.

Size dependent plasticity is a well-established component of dislocation theory, the effect is widely observed in metallic nano-indentation studies [31], and the trend has recently been highlighted in mechanical studies on lithium at length scales between 1 and 10  $\mu\text{m}$  [8,10,15]. The data we have presented in this paper quantify this, showing that on the  $\approx 200 \text{ nm}$  length scale relevant for lithium filaments, the hardness is in excess of 100 MPa. The flow stress of nanoscale lithium can be approximated as a third of the measured hardness [36], approximately 30 MPa.

Previous experimental work has demonstrated crack propagation by lithium deposition within the crack under a compressive stress – evidenced by subsequent viscoplastic extrusion of lithium out of the crack [3], a good example is reproduced in Fig. 4B. If lithium is under

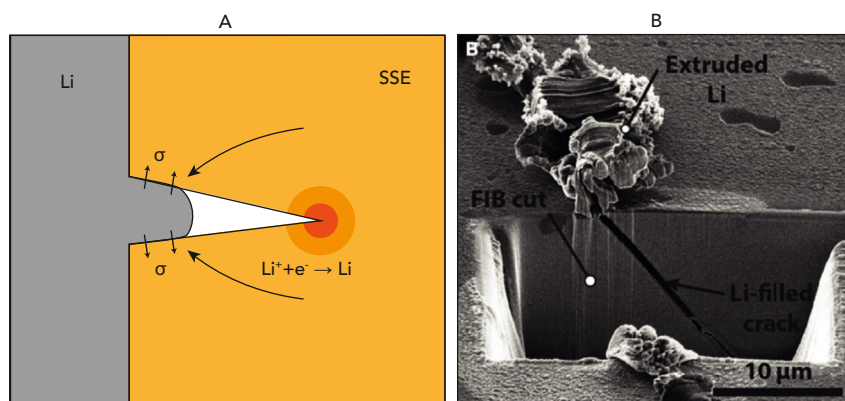


**Fig. 4.** Relevance of nanoscale hardness to solid electrolyte fracture, due to lithium plating within cracks. A – Schematic of stress concentration due to redistributed crack opening stress from lithium plated within a crack in a solid-state electrolyte (SSE). B – Image reproduced from Kazyak et al. [3] showing lithium-filled crack of width  $<500 \text{ nm}$  in high-density  $\text{Li}_7\text{La}_3\text{Zr}_2\text{O}_{12}$  (LLZO) and subsequent Li extrusion.

a compressive pressure, an equal opening pressure must be exerted on the solid electrolyte; this is shown schematically in Fig. 4A. As ceramic solid electrolytes are stiff, the crack opening forces are redistributed leading to a stress concentration at the crack tip. Considering the simple filled crack case, linear elastic fracture mechanics equations for an edge crack experiencing internal pressure can be used [37,38] ( $K_I = \Psi \sigma \sqrt{\pi a}$ , where  $K_I$  is the stress concentration at the crack tip,  $\sigma$  crack opening pressure,  $a$  crack length, and  $\Psi$  a geometry factor of approximately one). Solid electrolytes are typically stiff ceramics, with low bulk fracture toughness values ( $K_{Ic}$ ) in the range 0.5–1  $\text{MPa}\sqrt{\text{m}}$  [39–42], with the notable exception of LiPON – which seems to have a high fracture toughness [41]. Assuming a maximum flaw size of 5  $\mu\text{m}$ , a uniform crack opening pressure of 30 MPa is too small to cause catastrophic fracture in solid electrolyte materials ( $K_I 0.12 \text{ MPa}\sqrt{\text{m}} < K_{Ic}$ ).

There are three possible explanations for the observed fracture in ceramic solid electrolytes on lithium plating.

First, it may be for very high currents, the higher stresses evolved at higher strain rates than we have tested here or very small crack diameters (<100 nm) [43] are sufficient to drive fracture. A crack opening stress of 200 MPa and a crack length of 5  $\mu\text{m}$  will fracture materials with a fracture toughness below 0.8  $\text{MPa}\sqrt{\text{m}}$ . It may also be that the fracture toughness at grain boundaries in these materials is lower than in the bulk, as has been observed in other ceramics [44], so lower opening stresses drive fracture.

Second, to yield lithium out of a crack, forces at the lithium–ceramic interface will need to be overcome in addition to overcoming the material's intrinsic yield stress (von Mises yield criterion). The magnitude of the adhesion measured here suggests these forces may be significant. The situation is analogous to forging where the average pressure needed grows exponentially with the friction coefficient and aspect ratio.

Third, most experimental works demonstrating lithium filament propagation and concurrent electrolyte fracture show a progressive degradation over successive cycles, instead of catastrophic fracture on the first [1,3,45,46]. This matches the well-established concept of crack growth under a subcritical but cyclic load, where the crack growth per cycle in the main (stage II) regime is described by the Paris–Erdogan law. As such, cyclic stresses caused by lithium plating and stripping from within a crack on successive cycles will propagate the crack across the electrolyte. Below a threshold stress concentration amplitude, crack growth is negligible in ceramics – this threshold value is a materials property, which should be investigated for candidate solid electrolyte materials. There are no current studies of this type on solid electrolyte materials.

Further work is needed to model the mechanical interaction between lithium metal and solid-state electrolytes, and we hope the results in this work can inform these more accurate models. In the meantime, higher fracture toughness electrolytes should be pursued. The hardness results in this work suggest that electrolytes which can tolerate cyclic loads of the order of 100 MPa, for as many cycles as the battery is intended to perform, should be pursued.

#### 4. Concluding remarks

In this work, we have quantified the mechanics of lithium at the nanoscale by nanoindentation. Our measurements suggest stiffness tensor components of  $C_{11} = 13.3$ ,  $C_{12} = 11.2$ , and  $C_{44} = 8.8$  GPa. Clear size-dependent hardness is observed due to the stressed volume being small enough, so that few dislocations experience a shear stress and therefore less slip occurs than would for a bulk test. A hardness greater than 100 MPa is observed on the length scale of lithium filaments; this is two orders of magnitude higher than the bulk measured yield stress of 0.6 MPa [15]. Linear elastic fracture

mechanics suggest crack opening stresses of this order are likely to fracture current solid electrolyte materials due to their relatively low fracture toughness, especially over successive cycles.

#### Author contributions

Conceptualization, J.A., D.E.J.A., and M.P.; Methodology, J.A.; Investigation, J.A.; Writing – Original Draft, J.A.; Writing – Review Editing, J.A., D.E.J.A., and M.P.; Funding Acquisition, M.P.; Resources, D.E.J.A., M.P. Supervision, D.E.J.A. and M.P.

#### Data availability

Data will be made available on request.

#### Declaration of competing interest

The authors declare that they have no known competing financial interests or personal relationships that could have appeared to influence the work reported in this paper.

#### Acknowledgments

This work was supported by the Faraday Institution [grant numbers FIRG007, FIRG026, FIRG014 and FITG019-B]. Equipment including the indenter was funded by the Henry Royce Institute (through UK Engineering and Physical Science Research Council grant EP/R010145/1). The authors acknowledge Dr J E Darnbrough for initial work argon-ion polishing lithium for EBSD and Prof. A J Wilkinson for first suggesting microtome.

#### Appendix A. Supplementary data

Supplementary data to this article can be found online at <https://doi.org/10.1016/j.mtener.2022.101183>.

#### References

- [1] S. Hao, S.R. Daemi, T.M. Heenan, W. Du, C. Tan, M. Storm, C. Rau, D.J. Brett, P.R. Shearing, Tracking lithium penetration in solid electrolytes in 3D by in-situ synchrotron X-ray computed tomography, *Nano Energy* 82 (October 2020) 105744, <https://doi.org/10.1016/j.nanoen.2021.105744> doi: 10.1016/j.nanoen.2021.105744.
- [2] M. Pasta, D. Armstrong, Z.L. Brown, J. Bu, M.R. Castell, P. Chen, A. Cocks, S.A. Corr, E.J. Cussen, E. Darnbrough, V. Deshpande, C. Doerr, M.S. Dyer, H. El-Shinawi, N. Fleck, P. Grant, G.L. Gregory, C. Grovenor, L.J. Hardwick, J.T. Irvine, H.J. Lee, G. Li, E. Liberti, I. McClelland, C. Monroe, P.D. Nellist, P.R. Shearing, E. Shoko, W. Song, D.S. Jolly, C.I. Thomas, S.J. Turrell, M. Vestli, C.K. Williams, Y. Zhou, P.G. Bruce, 2020 roadmap on solid-state batteries, *J. Phys. Energy* 2 (3) (2020), 032008, <https://doi.org/10.1088/2515-7655/ab95f4>.
- [3] E. Kazyak, R. Garcia-Mendez, W.S. LePage, A. Sharafi, A.L. Davis, A.J. Sanchez, K.H. Chen, C. Haslam, J. Sakamoto, N.P. Dasgupta, Li penetration in ceramic solid electrolytes: operando microscopy analysis of morphology, propagation, and reversibility, *Matter* 2 (4) (2020) 1025–1048, <https://doi.org/10.1016/j.matt.2020.02.008>.
- [4] R. Schultz, *Lithium: Measurement of Young's Modulus*, Tech. Rep. November, Fermi National Accelerator Laboratory, 2002.
- [5] H.C. Nash, C.S. Smith, Single-crystal elastic constants of lithium, *J. Phys. Chem. Solid.* 9 (2) (1959) 113–118, [https://doi.org/10.1016/0022-3697\(59\)90201-X](https://doi.org/10.1016/0022-3697(59)90201-X).
- [6] T. Slotwinski, J. Trivisonno, Temperature dependence of the elastic constants of single crystal lithium, *J. Phys. Chem. Solid.* 30 (5) (1969) 1276–1278, [https://doi.org/10.1016/0022-3697\(69\)90386-2](https://doi.org/10.1016/0022-3697(69)90386-2).
- [7] R.A. Felice, J. Trivisonno, D.E. Schuele, Temperature and pressure dependence of the single-crystal elastic constants of Li and natural lithium, *Phys. Rev. B* 16 (12) (1977) 5173–5184.
- [8] C. Xu, Z. Ahmad, A. Aryanfar, V. Viswanathan, J.R. Greer, Enhanced strength and temperature dependence of mechanical properties of Li at small scales and its implications for Li metal anodes, *Proc. Natl. Acad. Sci. U. S. A.* 114 (1) (2017) 57–61, <https://doi.org/10.1073/pnas.1615733114>.
- [9] P.W. Bridgman, The electrical resistance of metals under pressure, *Proc. Am. Acad. Arts Sci.* 57 (3) (1922) 41–66.

- [10] E.G. Herbert, S.A. Hackney, N.J. Dudney, Nanoindentation of High-Purity Vapor Deposited Lithium Films: The Elastic Modulus, 2018, pp. 1335–1346, <https://doi.org/10.1557/jmr.2018.83>.
- [11] W.M. Robertson, D.J. Montgomery, Elastic modulus of isotopically-concentrated lithium, *Phys. Rev.* 117 (2) (1960) 440–442, <https://doi.org/10.1103/PhysRev.117.440>.
- [12] S. Tariq, K. Ammigan, P. Hurh, R. Schultz, Li material testing - fermilab antiproton source lithium collection lens, in: *Proceedings of the 2003 Particle Accelerator Conference*, 2003, pp. 1452–1454.
- [13] A. Masias, N. Felten, R. Garcia-Mendez, J. Wolfenstine, J. Sakamoto, Elastic, plastic, and creep mechanical properties of lithium metal, *J. Mater. Sci.* 54 (3) (2019) 2585–2600, <https://doi.org/10.1007/s10853-018-2971-3>.
- [14] M. Kamaya, A procedure for estimating Young's modulus of textured polycrystalline materials, *Int. J. Solid Struct.* 46 (13) (2009) 2642–2649, <https://doi.org/10.1016/j.ijsolstr.2009.02.013>, doi:10.1016/j.ijsolstr.2009.02.013.
- [15] C.D. Fincher, D. Ojeda, Y. Zhang, G.M. Pharr, M. Pharr, Mechanical properties of metallic lithium: from nano to bulk scales, *Acta Mater.* 186 (2020) 215–222, <https://doi.org/10.1016/j.actamat.2019.12.036>.
- [16] D. Hull, H.M. Rosenberg, The deformation of lithium, sodium and potassium at low temperatures: tensile and resistivity experiments, *Phil. Mag.* 4 (39) (1959) 303–315, <https://doi.org/10.1080/14786435908233342>.
- [17] W.S. LePage, Y. Chen, E. Kazyak, K.H. Chen, A.J. Sanchez, A. Poli, E.M. Arruda, M.D. Thouless, N.P. Dasgupta, Lithium mechanics: roles of strain rate and temperature and implications for lithium metal batteries, *J. Electrochem. Soc.* 166 (2) (2019) 89–97, <https://doi.org/10.1149/2.0221902jes>.
- [18] J.Z. Lee, T.A. Wynn, M.A. Schroeder, J. Alvarado, X. Wang, K. Xu, Y.S. Meng, Cryogenic focused ion beam characterization of lithium metal anodes, *ACS Energy Lett.* 4 (2) (2019) 489–493, <https://doi.org/10.1021/acseenergylett.8b02381>.
- [19] S. Shim, H. Bei, M.K. Miller, G.M. Pharr, E.P. George, Effects of focused ion beam milling on the compressive behavior of directionally solidified micropillars and the nanoindentation response of an electropolished surface, *Acta Mater.* 57 (2) (2009) 503–510, <https://doi.org/10.1016/j.actamat.2008.09.033>, doi:10.1016/j.actamat.2008.09.033.
- [20] J.F. Ziegler, M.D. Ziegler, J.P. Biersack, SRIM - the stopping and range of ions in matter (2010), *Nucl. Instrum. Methods Phys. Res. Sect. B Beam Interact. Mater. Atoms* 268 (11–12) (2010) 1818–1823, <https://doi.org/10.1016/j.nimb.2010.02.091>, doi:10.1016/j.nimb.2010.02.091.
- [21] H. Azza, N. Selhaoui, A. Iddoudi, L. Bouirden, Thermodynamic reassessment of the gallium–lithium phase diagram, *J. Phase Equilibria Diffus.* 38 (5) (2017) 788–795, <https://doi.org/10.1007/s11669-017-0567-2>.
- [22] B.R. Rogne, C. Thaulow, Strengthening mechanisms of iron micropillars, *Phil. Mag.* 95 (16–18) (2015) 1814–1828, <https://doi.org/10.1080/14786435.2014.984004>.
- [23] J.J. Vlassak, W. Nix, Measuring the elastic properties of materials by means of indentation, *J. Mech. Phys. Solids* 42 (8) (1994) 1223–1245.
- [24] B. Merle, W.H. Higgins, G.M. Pharr, Critical issues in conducting constant strain rate nanoindentation tests at higher strain rates, *J. Mater. Res. (i)* (2019), <https://doi.org/10.1557/jmr.2019.292>.
- [25] P.S. Phani, W.C. Oliver, G.M. Pharr, Understanding and modeling plasticity error during nanoindentation with continuous stiffness measurement, *Mater. Des.* 194 (2020), 108923, <https://doi.org/10.1016/j.matdes.2020.108923>, doi:10.1016/j.matdes.2020.108923.
- [26] W. Oliver, G. Pharr, An improved technique for determining hardness and elastic modulus using load and displacement sensing indentation experiments, *J. Mater. Res.* 7 (6) (1992) 1564–1583, <https://doi.org/10.1557/jmr.1992.1564>.
- [27] M. Kitta, H. Sano, Real-time observation of Li deposition on a Li electrode with operant atomic force microscopy and surface mechanical imaging, *Langmuir* 33 (8) (2017) 1861–1866, <https://doi.org/10.1021/acs.langmuir.6b04651>.
- [28] T. Tabata, P. Andreo, K. Shinoda, An analytic formula for the extrapolated range of electrons in condensed materials, *Nucl. Instrum. Methods Phys. Res. Sect. B Beam Interact. Mater. Atoms* 119 (4) (1996) 463–470, [https://doi.org/10.1016/S0168-583X\(96\)00687-8](https://doi.org/10.1016/S0168-583X(96)00687-8).
- [29] F. Shi, A. Pei, A. Vailionis, J. Xie, B. Liu, J. Zhao, Y. Gong, Y. Cui, Strong texturing of lithium metal in batteries, *Proc. Natl. Acad. Sci. U. S. A.* 114 (46) (2017) 12138–12143, <https://doi.org/10.1073/pnas.1708224114>.
- [30] N. Brodusch, K. Zaghib, R. Gauvin, Electron backscatter diffraction applied to lithium sheets prepared by broad ion beam milling, *Microsc. Res. Tech.* 78 (1) (2015) 30–39, <https://doi.org/10.1002/jemt.22441>.
- [31] W.D. Nix, H. Gao, Indentation size effects in crystalline materials: a law for strain gradient plasticity, *J. Mech. Phys. Solid.* 46 (3) (1998) 411–425, [https://doi.org/10.1016/S0022-5096\(97\)00086-0](https://doi.org/10.1016/S0022-5096(97)00086-0).
- [32] G.M. Pharr, E.G. Herbert, Y. Gao, The indentation size effect: a critical examination of experimental observations and mechanistic interpretations, *Annu. Rev. Mater. Res.* 40 (2009) 271–292, <https://doi.org/10.1146/annurev-matsci-070909-104456>.
- [33] G. Ziegenhain, H.M. Urbassek, A. Hartmaier, Influence of crystal anisotropy on elastic deformation and onset of plasticity in nanoindentation: a simulation study, *J. Appl. Phys.* 107 (6) (2010), <https://doi.org/10.1063/1.3340523>.
- [34] Y. Jin, B. Zhu, Z. Lu, N. Liu, J. Zhu, Challenges and recent progress in the development of Si anodes for lithium-ion battery, *Adv. Energy Mater.* 7 (23) (2017) 1–17, <https://doi.org/10.1002/aenm.201700715>.
- [35] Y. Jiang, D.S. Grierson, K.T. Turner, Flat punch adhesion: transition from fracture-based to strength-limited pull-off, *J. Phys. Appl. Phys.* 47 (32) (2014), <https://doi.org/10.1088/0022-3727/47/32/325301>.
- [36] J.T. Busby, M.C. Hash, G.S. Was, The relationship between hardness and yield stress in irradiated austenitic and ferritic steels, *J. Nucl. Mater.* 336 (2–3) (2005) 267–278, <https://doi.org/10.1016/j.jnucmat.2004.09.024>.
- [37] I.N. Sneddon, H.A. Elliot, The opening of a Griffith crack under internal pressure, *Q. Appl. Math.* 4 (3) (1946) 262–267, <https://doi.org/10.1090/qam/17161>.
- [38] M. Sakamoto, An elastic layer with a penny-shaped crack subjected to internal pressure, *JSME International Journal Series A* 46 (1) (2003) 10–14, <https://doi.org/10.1299/jsmea.46.10>, [http://www.jstage.jst.go.jp/article/jsmea/46/1/46\\_1\\_10/\\_article](http://www.jstage.jst.go.jp/article/jsmea/46/1/46_1_10/_article).
- [39] J. Wolfenstine, J.L. Allen, J. Sakamoto, D.J. Siegel, H. Choe, Mechanical behavior of Li-ionconducting crystalline oxide-based solid electrolytes: a brief review, *Ionics* 24 (5) (2018) 1271–1276, <https://doi.org/10.1007/s11581-017-2314-4>.
- [40] S.D. Jackman, R.A. Cutler, Effect of microcracking on ionic conductivity in LATP, *J. Power Sources* 218 (2012) 65–72, <https://doi.org/10.1016/j.jpowsour.2012.06.081>, doi:10.1016/j.jpowsour.2012.06.081.
- [41] S. Kalnaus, A.S. Westover, M. Kornbluth, E. Herbert, N.J. Dudney, Resistance to fracture in the glassy solid electrolyte Lipon, *J. Mater. Res.* 36 (4) (2021) 787–796, <https://doi.org/10.1557/s43578-020-00098-x>.
- [42] J.F. Nonemacher, S. Naqash, F. Tietz, J. Malzbender, Micromechanical assessment of Al/Y-substituted NASICON solid electrolytes, *Ceram. Int.* 45 (17) (2019) 21308–21314, <https://doi.org/10.1016/j.ceramint.2019.07.114>.
- [43] L. Zhang, T. Yang, C. Du, Q. Liu, Y. Tang, J. Zhao, B. Wang, T. Chen, Y. Sun, P. Jia, H. Li, L. Geng, J. Chen, H. Ye, Z. Wang, Y. Li, H. Sun, X. Li, Q. Dai, Y. Tang, Q. Peng, T. Shen, S. Zhang, T. Zhu, J. Huang, Lithium Whisker Growth and Stress Generation in an in Situ Atomic Force Microscope–Environmental Transmission Electron Microscope Set-Up, 2020, <https://doi.org/10.1038/s41565-019-0604-x>, 2.
- [44] R. Xu, H. Sun, L.S. de Vasconcelos, K. Zhao, Mechanical and structural degradation of LiNi<sub>x</sub>Mn<sub>y</sub>Co<sub>z</sub>O<sub>2</sub> cathode in Li-ion batteries: an experimental study, *J. Electrochem. Soc.* 164 (13) (2017) A3333–A3341, <https://doi.org/10.1149/2.1751713jes>, <https://iopscience.iop.org/article/10.1149/2.1751713jes>.
- [45] Z. Ning, D.S. Jolly, G. Li, R. De Meyere, S.D. Pu, Y. Chen, J. Kasemchainan, J. Ihli, C. Gong, B. Liu, D.L. Melvin, A. Bonnin, O. Magdysyuk, P. Adamson, G.O. Hartley, C.W. Monroe, T.J. Marrow, P.G. Bruce, Visualizing plating-induced cracking in lithium-anode solid-electrolyte cells, *Nat. Mater.* 20 (8) (2021) 1121–1129, <https://doi.org/10.1038/s41563-021-00967-8>, doi:10.1038/s41563-021-00967-8.
- [46] L. Porz, T. Swamy, B.W. Sheldon, D. Rettenwander, T. Frömling, H.L. Thaman, S. Berendts, R. Uecker, W.C. Carter, Y.-M. Chiang, Mechanism of lithium metal penetration through inorganic solid electrolytes, *Adv. Energy Mater.* 7 (20) (2017), <https://doi.org/10.1002/aenm.201701003>, 10.